Probes for investigating the effect of magnetic field, field orientation, temperature and strain on the critical current density of anisotropic high-temperature superconducting tapes in a split-pair 15 T horizontal magnet

P. Sunwong, J. S. Higgins, and D. P. Hampshire

Articles you may be interested in

Near-isotropic performance of intrinsically anisotropic high-temperature superconducting tapes due to self-assembled nanostructures
Appl. Phys. Lett. **93**, 172512 (2008); 10.1063/1.3009286

Review of GeGaAs Thermometers and Multisensors for Measurement of Temperature and Magnetic Field in Cryogenic Applications
AIP Conf. Proc. **850**, 1595 (2006); 10.1063/1.2355317

Critical current versus strain measurement up to 21 T and 1000 A of long length superconducting wires and tapes
Rev. Sci. Instrum. **76**, 093901 (2005); 10.1063/1.2018608

Phase Formation and Critical Current Density of AgSheathed Bi2223 Tapes with Insulating SrVO Barriers
AIP Conf. Proc. **711**, 612 (2004); 10.1063/1.1774621

A probe for investigating the effects of temperature, strain, and magnetic field on transport critical currents in superconducting wires and tapes
Rev. Sci. Instrum. **71**, 4521 (2000); 10.1063/1.1324734

Probes for investigating the effect of magnetic field, field orientation, temperature and strain on the critical current density of anisotropic high-temperature superconducting tapes in a split-pair 15 T horizontal magnet

P. Sunwong, J. S. Higgins, and D. P. Hampshire
Superconductivity Group, Centre for Materials Physics, Department of Physics, University of Durham, Durham DH1 3LE, United Kingdom

We present the designs of probes for making critical current density (J_c) measurements on anisotropic high-temperature superconducting tapes as a function of field, field orientation, temperature and strain in our 40 mm bore, split-pair 15 T horizontal magnet. Emphasis is placed on the design of three components: the vapour-cooled current leads, the variable temperature enclosure, and the springboard-shaped bending beam sample holder. The vapour-cooled brass critical-current leads used superconducting tapes and in operation ran hot with a duty cycle (D) of ∼0.2. This work provides formulae for optimising cryogenic consumption and calculating cryogenic boil-off, associated with current leads used to make J_c measurements, made by uniformly ramping the current up to a maximum current (I_{max}) and then reducing the current very quickly to zero. They include consideration of the effects of duty cycle, static helium boil-off from the magnet and Dewar (b'), and the maximum safe temperature for the critical-current leads (T_{max}). Our optimized critical-current leads have a boil-off that is about 30% less than leads optimized for magnet operation at the same maximum current. Numerical calculations show that the optimum cross-sectional area (A) for each current lead can be parameterized by $L I_{max}/A = [1.46 D^{-0.18} L^{0.4} (T_{max} - 300)^{0.25 D^{-0.09}} + 750(b'/I_{max}) D^{10^{-3} I_{max} - 2.87 b'}] \times 10^6$ A m^{-1} where L is the current lead's length and the current lead is operated in liquid helium. An optimum A of 132 mm^2 is obtained when $I_{max} = 1000$ A, $T_{max} = 400$ K, $D = 0.2$, $b' = 0.3$ l h^{-1} and $L = 1.0$ m. The optimized helium consumption was found to be 0.7 l h^{-1}. When the static boil-off is small, optimized leads have a boil-off that can be roughly parameterized by: $b/I_{max} \approx (1.35 \times 10^{-3}) D^{0.41}$ l h^{-1} A^{-1}. A split-current-lead design is employed to minimize the rotation of the probes during the high current measurements in our high-field horizontal magnet. The variable-temperature system is based on the use of an inverted insulating cup that operates above 4.2 K in liquid helium and above 77.4 K in liquid nitrogen, with a stability of ±80 mK to ±150 mK. Uniaxial strains of −1.4% to 1.0% can be applied to the sample, with a total uncertainty of better than ±0.02%, using a modified bending beam apparatus which includes a copper beryllium springboard-shaped sample holder. © *2014 AIP Publishing LLC.* [http://dx.doi.org/10.1063/1.4881235]

I. INTRODUCTION

Critical current density (J_c) is probably the most important property of a superconductor from the perspective of technological applications. Low temperature superconductors (LTSs) have been studied intensively as a function of magnetic field (B), temperature (T), and strain (ε)[1–3] with dedicated probes. LTSs are broadly isotropic and either ductile or can be produced using wind-and-react techniques so that helical-shaped samples can be formed for measuring J_c in vertical superconducting magnets in high fields. The helical configuration ensures that the heat and voltage generated near the current-lead joints are far from the voltage taps. However, most high-temperature superconductors (HTSs) are anisotropic so magnet engineers require knowledge of the anisotropy of J_c—in particular the anisotropy associated with how the angle of the magnetic field with respect to tape surface affects J_c while the transport current remains orthogonal to the field—so helical sample holders are less useful. Furthermore, many HTS materials cannot be obtained in

unstrained helical form (e.g., 2G YBa$_2$Cu$_3$O$_7$ tapes or 3G DI-BiSCCO tapes[4]) but are currently only available unstrained as straight conductors. For transport measurements using small currents, these straight materials can be rotated in standard vertical magnets using ingenious experimental design.[5] However, as the sample currents required approach and exceed 1000 A in high magnetic fields, low E-field high-J_c measurements are best done in a horizontal split pair magnet. In this work, we present the important design features of a $J_c(B, T, \theta, \varepsilon)$ probe for making critical current measurements on anisotropic high-temperature superconducting tapes as a function of field, field angle (θ) between the magnetic field and surface of the tape (in quasi single crystal tapes this is usually arbitrarily taken with respect to the crystallographic *a-b* plane), temperature and strain for use in our split-pair 15 T (40 mm bore) horizontal superconducting magnet. Our approach was to build and optimize a $J_c(B, T, \theta)$ probe and then optimize the design of a $J_c(B, T, \theta, \varepsilon)$ probe—both are presented in this paper.

The broad themes of this paper are structured as follows: Sec. II provides a broad description of the $J_c(B, T, \theta)$ probe with some guiding principles for design; Sec. III considers optimization of current leads for use in liquid helium. An important aspect of this paper is optimization of helium consumption, because scarcity of helium gas is becoming a serious issue.[6] Wilson[7] has analysed magnet current lead design and demonstrated that the minimum helium boil-off is about 2.9×10^{-3} $1h^{-1}A^{-1}$ (for two leads) independent of material used in the approximation that it obeys the Wiedemann-Franz law. The optimum LI/A varies from material to material. High-conductivity copper and phosphorous deoxidized copper have optimum LI/A values of 26×10^6 A m^{-1} and 3.5×10^6 A m^{-1}, respectively. Wilson's work considers steady state conditions for magnet current leads where the current is constant and the current leads are in thermal equilibrium. It shows that at optimum design the temperature of the leads remains at and below room temperature. Operation of hot current leads has been studied in several systems including the pulse mode operation of poloidal field coils of tokamak and low-duty cycling of magnets.[8,9] Such studies consider how to minimize the time-averaged heat leak to reduce helium consumption. In this work, we investigate behaviour of critical-current leads for J_c measurements, where the current is not constant as in magnets, but linearly increases with time over about 200 s up to J_c and then rapidly reduces to zero. The effects of duty cycle, maximum current to be measured, static boil-off and the incorporation of additional superconducting tapes as part of the leads are all considered in our drive to minimize helium boil-off. Not surprisingly, we find that the optimum current lead design is different for magnet operation and critical current measurements. The paper provides some formulae that quantify the reduction in cryogenic consumption (which for our measurements is about 30%). They consider the ramping current, the duty cycle, and include "hot" current lead operation at the very highest currents of the ramp; Sec. IV considers the design and operation of a variable temperature enclosure. Fixed temperature J_c measurements are routinely completed in a cryogen such as liquid helium (at 4.2 K) and liquid nitrogen (at 77.4 K). Standard techniques used to vary and control the temperature include cryogenic vapour pressure control (i.e., liquid refrigerant pumping),[10,11] use of cryocoolers,[12–14] and use of resistance heaters.[1,15,16] We require a variable-temperature system that provides a large temperature range and is simple and robust. The University of Twente[2,17] pioneered using the inverted cup which activates by turning heaters on to provide a variable-temperature gas environment for J_c measurements. This technique provides a large temperature range (above 4.2 K for measurements in liquid helium and above 77.4 K for measurements in liquid nitrogen). The design and optimization of the inverted cup is discussed along with calculations of heat transfer from all component parts as well as temperature stability inside the cup; Sec. V considers the broad design of the $J_c(B, T, \theta, \varepsilon)$ probe; Sec. VI considers applying and controlling the axial strain on a superconductor while J_c is measured. Axial strain has long been of interest in the study of LTS and inevitably, this interest has followed to HTS wires and tapes. Ekin completed a detailed

study of the effect of tensile strain on commercial high J_c conductors.[18] In general, tensile measurements are probably now most sensitively made using Nyilas extensometers.[19,20] However, measuring and understanding superconductors in compression is also necessary. Walters introduced a spring[21] (WASP) design to investigate long-length samples at low E-field (high sensitivity) under both compression and tension, in high fields. The basic principle of the WASP/bending beam is that the sample is soldered to a sample holder and either compressive and tensile strain applied by twisting or bending it and strain gauges used to determine the strain in the sample. Cheggour and Hampshire developed a variable temperature WASP.[1,22] Access to variable-temperature and variable-strain measurements (in one probe) on a single sample enabled a resolution of the apparent contradiction between strain scaling (found at fixed temperature)[18] and temperature scaling (at fixed strain).[23–26] This led to a general scaling law[23,24,27] for LTS materials which includes a $1/\kappa^2$ term[28] (κ: Ginzburg-Landau constant) that gives best fits to the data for Nb$_3$Sn[23,29] and Nb$_3$Al[30] and is consistent with computational data[31] and general analytic forms.[32,33] An excellent bending beam apparatus was also developed at the University of Twente for short samples of LTS wires.[34–36] Its design gives access to variable temperature, variable strain J_c measurements in the very highest dc magnetic fields (in vertical magnets) available, but has the drawback of relatively high E-field baselines (short samples with finite current transfer lengths[37,38]). Our research aims broadly include contributing to finding HTS scaling laws analogous to the ones available for LTS materials and to optimizing HTS for high-field applications such as MRI[39] and fusion tokamaks.[40] Given that at present the best HTS materials are generally only available in straight form, a helical WASP is not practical. We present here the design and operation of a long vertical bending beam (springboard-shaped sample holder), that is, used for straight samples in our 40 mm bore horizontal-magnet. Although horizontal magnets are more expensive than vertical magnets of equivalent peak field and bore-size, the approach taken here better facilitates low E-field, high current ($\sim$1000 A), J_c measurements on anisotropic HTS materials as a function of magnetic field orientation (as well as temperature and strain). Simply rotating the probes changes the orientation of the sample with respect to the applied field (while maintaining the current leads fixed with respect to the sample); In Sec. VII, the performance of the $J_c(B, T, \theta, \varepsilon)$ probe is demonstrated by presenting a range of J_c data obtained from YBCO tapes.

II. DESCRIPTION OF $J_c(B, T, \theta)$ PROBE

Figure 1 shows a diagram of the probe designed for investigating the effects of magnetic field, field orientation, and temperature on the critical current density of HTS tapes. In operation, the upper part becomes the hottest part of the probe and is most likely to burn out because the heat from the room temperature environment and the Joule heating from the current leads are at their maxima. The head of the probe is designed so that when the current terminals and the upper part of the current leads become hot there are no contiguous components that are likely to fail when hot (e.g., melt). The current
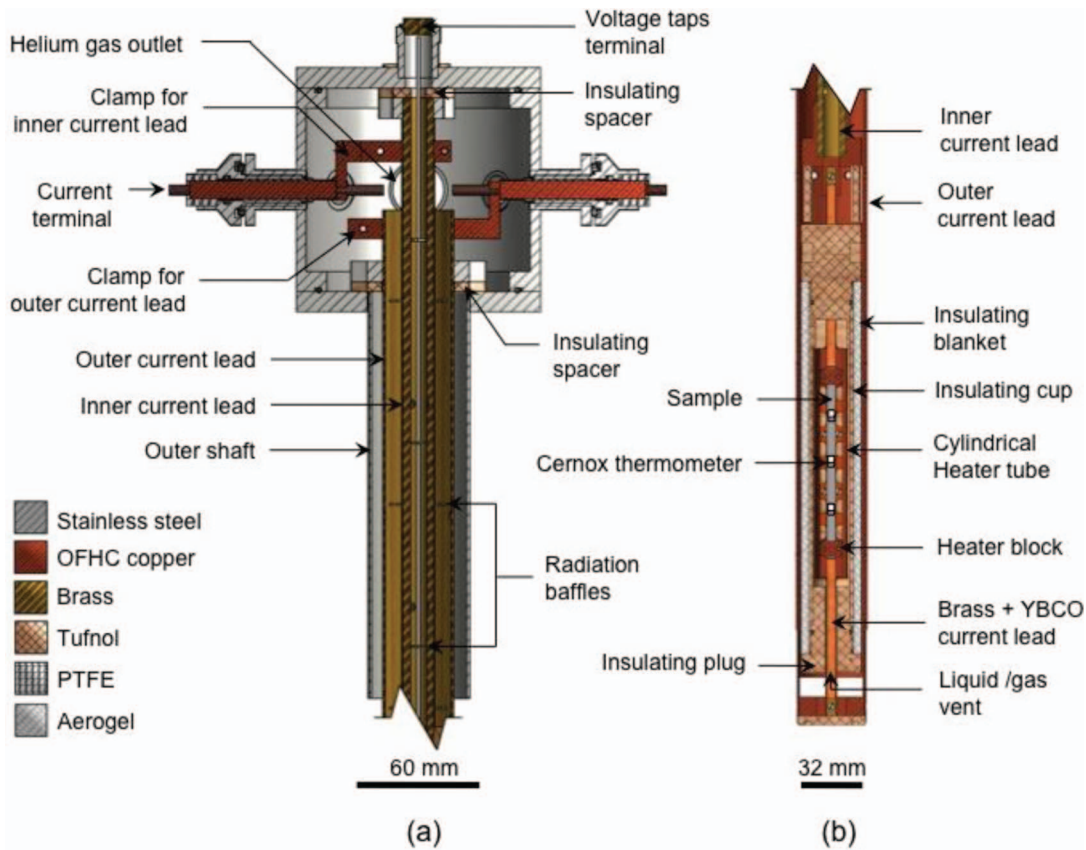
FIG. 1. Diagram of the $J_c(B, T, \theta)$ probe (a) the top part of the probe including cylindrical current lead tubes and (b) the final design of the variable-temperature cup and insulating plug and vent.

leads themselves are made from two cylindrical brass tubes with different wall thicknesses. Brass was chosen because it has a much lower thermal conductivity than copper at low temperature (two orders of magnitude lower at temperatures below 30 K) and its resistivity is less temperature dependent than an alternative such as high-purity copper.[7] This in prac-

tice means that current leads can be reasonably robust for a given low heat leak and make it a common choice for magnet current leads. The important properties of materials and cryogens used in this work are summarized in Table I. The cylindrical shape of the leads was chosen to provide good mechanical strength and a large surface area for gas cooling.

TABLE I. Density, thermal conductivity, specific heat capacity, and resistivity of materials and cryogens.

Material/gas	Density (kg m^{-3})			Specific heat capacity (J kg^{-1} K^{-1})			Thermal conductivity (W m^{-1} K^{-1})			Electrical resistivity (10^{-8} Ω m)		
	4.2 K	77.4 K	293 K	4.2 K	77.4 K	293 K	4.2 K	77.4 K	293 K	4.2 K	77.4 K	293 K
Copper (RRR = 50)[a,b]			8950	0.11	196	389	334	515	393	0.03	0.2	1.7
Brass[a,b]			8520	0.15	216	377	2.08	39.8	109	4.2	4.7	6.9
Copper beryllium[a,b]			8330			419	1.97	36.3	105			7.8
Stainless steel (304)[a,b]			7860	2	204	470	0.272	7.92	15.1	50	52	74
Polyimide[a,b]			1430	1	338	747	0.011	0.126	0.191			
Phenolic[b]			1100			1260	~0.1	0.184	0.281			
Tufnol[c]			1350			1500			0.37			
Aerogel[d]			150			1000	~0.01	0.010	0.014			
Helium (gas)[e,f]	16.76	0.632	0.166	9080	5190	5190	0.009	0.063	0.154			
Nitrogen (gas)[e,g]	...	4.612	1.165	...	1120	1040	...	0.007	0.025			

[a]Reference 16.
[b]Reference 49.
[c]The properties shown are for Carp Brand Tufnol which is made from phenolic resin and cotton fabric.[50]
[d]Reference 51.
[e]Reference 52.
[f]Boiling point of helium is 4.230 K at 1 atm. Latent heat of vapourization is 20.75 kJ kg^{-1} (Ref. 16) so 1 W is equivalent to 1.4 l h^{-1}.
[g]Boiling point of nitrogen is 77.35 K at 1 atm. Latent heat of vapourization is 199.2 kJ kg^{-1} (Ref. 16) so 1 W is equivalent to 22 ml h^{-1}.
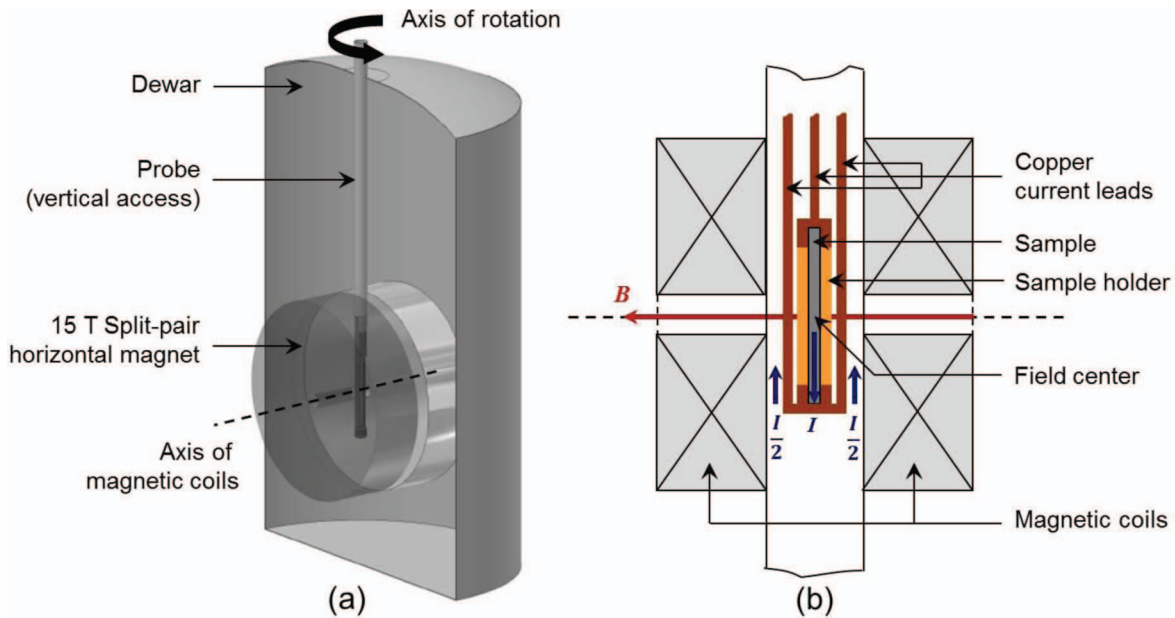
FIG. 2. Schematic diagram of (a) the 15 T split-pair horizontal magnet system and (b) the split-current-lead design.

The current leads each have a 2-mm slit along their lengths (not shown) to prevent large Eddy currents occurring while sweeping the magnet (wasting cryogen) and in the event that the magnet quenches, to avoid melting the leads. Not shown are small Tufnol reinforcing structures that hold the cylindrical current lead tubes in shape. Figure 1(b) shows the inverted cup with its insulating plug (and vent) that provided the variable-temperature environment for the sample. The outer diameter of the cup was 32 mm so the probe can be inserted vertically into the 40 mm bore of our horizontal magnet system. The angular measurements were performed by rotating the probe to change the relative orientation between the horizontal field and the sample's flat surface. A schematic diagram of Durham's 15 T split-pair horizontal magnet is shown in Fig. 2 including the split-current-lead design for measurements in such high-field systems. Most parts of the probe were made from stainless steel, oxygen-free high conductivity copper (OFHC), brass, Tufnol, and aerogel as discussed below.

III. HIGH-CURRENT LEADS

A. Split-current-lead design

Measurements on isotropic LTS are usually made in vertical magnets where the current leads are parallel to the stray field of the magnet and hence there is no force on them.[41] In contrast, the current leads of probes in horizontal magnets are orthogonal to the stray field of the magnet so the forces on them can be large and the torque associated with the large Lorentz force can twist the bottom part of the probe even when the top part of the probe is fixed. The split-current-lead design has been used in our group[42] to minimize the torque as well as the self-field produced at the sample by the sample current. The experimental apparatus is illustrated in Fig. 2(b). The current lead that is attached to the bottom of the sample is split into two parts while the other (central) lead attached to the top of the sample remains a single lead. Figures 3 and 4

show the performance of the split-current-lead design we originally used[42] in the $J_c(B, T, \theta)$ probe and the split-current-lead design implemented in this work for the $J_c(B, T, \theta, \varepsilon)$ probe. The angular measurements in both probes were performed on DI-BiSCCO tapes at 4.2 K and the data are plotted up to values of current which generated electric fields of 100 μV m^{-1} across the voltage taps (i.e., where J_c is determined). The angle was monitored by a Hall sensor during the J_c measurements. Figure 3 shows that the $J_c(B, T, \theta)$ probe twisted up to 3.8° at a starting angle of $\theta = 10°$ due to the torque associated with unbalanced currents in the two parts (which in principle can be reduced by actively balancing the currents). These data can be reduced to a single universal curve consistent with a torque twisting the probe. However, the change in the angle of the $J_c(B, T, \theta, \varepsilon)$ probe (i.e., final design in Fig. 4) during J_c measurements was found to
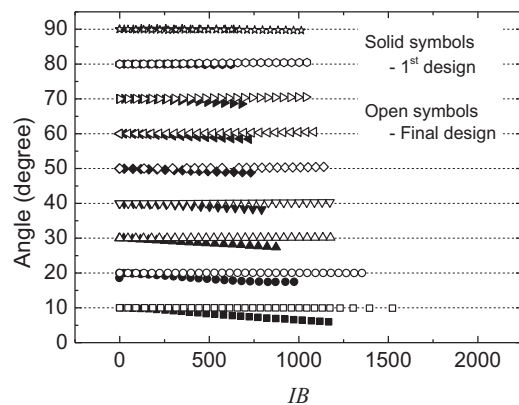

FIG. 3. Measurements of the instantaneous angle between magnetic field and the sample's surface as a function of the product of the current and the applied magnetic field for J_c measurements on a DI-BiSCCO tape at 4.2 K at different starting angles. The applied magnetic field was 3 T for the data obtained for the first design and 14 T for the final design. The data for each starting angle are plotted up to values of the current at which the electric field was 100 μV m^{-1} across the voltage taps.
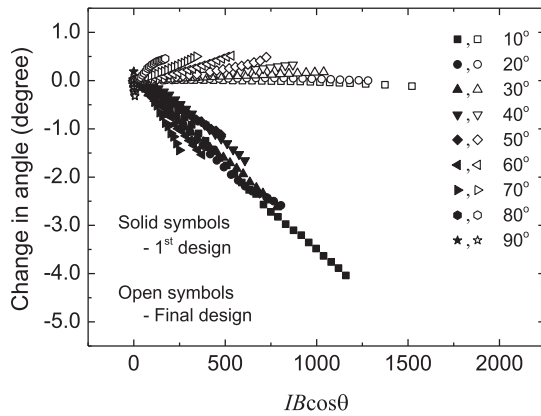
FIG. 4. Data from Fig. 3 replotted as the change in the angle during the J_c measurement as a function of the product of the current (I), the applied magnetic field (B), and the cosine of the instantaneous angle between magnetic field and the sample's surface at different starting angles.

be much smaller and not due to a simple torque (no universal behaviour). We attribute the reduction in twisting achieved to better balancing of the current in the split leads, the increased stiffness of the $J_c(B, T, \theta, \varepsilon)$ probe, and the flexibility of the split-current leads (so that the current leads were deformed rather than rotating the probe). Figure 5 shows the change in the measured component of the field normal to the sample surface for different starting angles at 80 A which is a result of the Lorentz force associated with current flowing in the sample itself. B_n decreased when the angle was less than $\sim 15°$ and increased otherwise. The maximum increase was found at $\sim 50°$. We attribute these changes to the Lorentz force moving the sample in a plane which has a spatial field variation (inset).

B. Optimization of the critical-current leads

The cross-sectional area of each current lead (A) that has one end at room temperature and the other end at cryogenic

temperatures can be optimized by considering the important of heat transfer. The generalized one-dimensional transient heat transfer equation for *one* vapour-cooled current lead is given by[7,43]

$$\frac{d}{dx}\left(\kappa(T)A\frac{dT}{dx}\right) - fm(t)c_p\frac{dT}{dx} + \frac{I^2(t)\rho_n(T)}{A}$$
$$= A\delta c(T)\frac{dT}{dt}, \qquad (1)$$

where T is the temperature in kelvin, x is the distance in meters along the current lead, κ is thermal conductivity of the current lead in $\mathrm{W\,m^{-1}\,K^{-1}}$, m is the mass flow of cryogen gas in $\mathrm{kg\,s^{-1}}$, I is the current flowing in amperes, f is the efficiency of heat transfer between the current lead and the gas, c_p is the specific heat capacity of the cryogen gas at constant pressure in $\mathrm{J\,kg^{-1}\,K^{-1}}$, and ρ_n, δ, and c are the electrical resistivity, density, and specific heat capacity of the current leads in $\Omega\,\mathrm{m}$, $\mathrm{kg\,m^{-3}}$, and $\mathrm{J\,kg^{-1}\,K^{-1}}$, respectively. Equation (1) includes the effects of heat conduction along the current lead, heat transfer from the current lead to the gas, and Joule heating of the current lead carrying the current I. Radiative heat transfer inside the cryostat has been ignored.[8,9] A schematic diagram of a current lead and the heat transfer mechanisms is provided in Fig. 6. The mass flow is found from the conductive heat transfer into the cryogen at the bottom end, $m(t) = (\kappa A/c_l)dT/dx|_{x=0}$, where c_l is the latent heat of vapourization in $\mathrm{J\,kg^{-1}}$. Accurate calculation also requires the inclusion of static boil-off of the cryostat (m_{sta}) and any additional Joule heating from elements directly immersed in the cryogen. An expression for the total cryogen boil-off for one current lead is therefore

$$m(t) = \frac{\kappa A}{c_l}\frac{dT}{dx}\bigg|_{x=0} + \frac{1}{2}\left(\frac{I^2(t)R}{c_l} + m_{\mathrm{sta}}\right), \qquad (2)$$
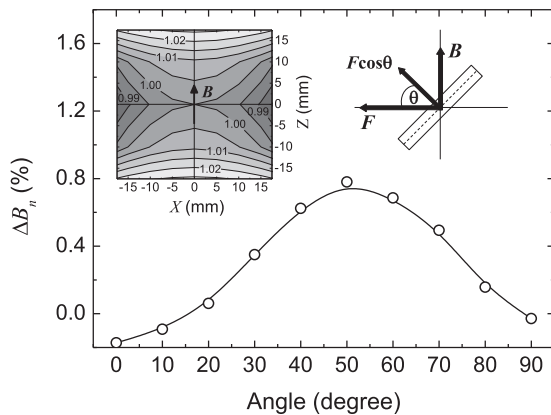

FIG. 5. Change in the normal field component at the sample when the current is at 80 A as a function of the starting angle between magnetic field and the sample's surface for the J_c measurements in this work. The inset shows the normalized magnetic field profile of Durham's split-pair horizontal magnet along the x-z plane which is the plane of the sample's cross-section. Movement of the sample (i.e., change in the normal field component) is attributed to effects of the normal force component ($F\cos\theta$).
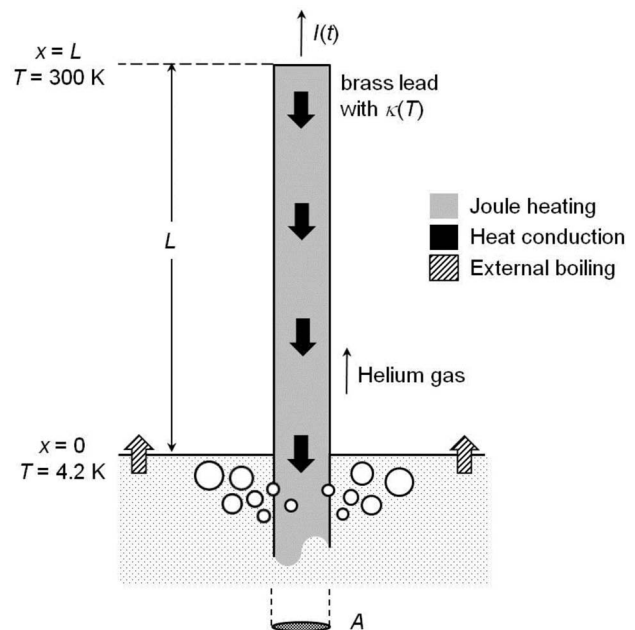

FIG. 6. Schematic diagram of a vapour-cooled brass current lead and heat transfer considerations for measurements in liquid helium.

where R is the total resistance of all parts immersed in the cryogen. The contribution of all static (primarily heat conduction into the Dewar) or sample boil-off (Joule heating) is assumed to be equally distributed among the two current leads. For best practice, R is generally minimized by using high purity copper or adding superconducting material for that part of the electrical circuit immersed in liquid cryogen, so in most of this paper we shall set R to zero.

The efficiency of heat transfer is by definition given by $f = (T - \Delta T)/T$ where ΔT is the difference between the temperature of the gas and the current lead at the same height.[7] It is physically dependent on the geometry of the current leads, the mass flow of the cryogen and the physical properties of the gas itself which vary along the current leads because of their temperature dependence. By taking into account the shape of the current leads, the cooling term can be written as a convective heat transfer term, $hP'(T - T_g)$, which includes gas temperature (T_g) and cooled perimeter (P'). h is the heat transfer coefficient which is $\cong 4\kappa_g/D'$ for a cylindrical pipe where κ_g is the thermal conductivity of the gas, $D' \cong 4A'/P'$ is the hydraulic diameter, and A' is the cross-sectional area of the pipe. Taken together, f can be written as a function of h where[7]

$$f = \left[1 + \frac{m(t)c_p dT/dx}{hP'T}\right]^{-1}. \qquad (3)$$

Equation (3) describes the effects of gas properties, temperature variation, and geometry of the current lead on the efficiency of heat transfer. A typical value for f from our measurements is between 0.8 and 1.0 which suggests efficient heat transfer. Hence in order to simplify our analysis, we have set $f = 1$ (perfect heat transfer) in the computation here. Cylindrical current lead tubes were used to try to ensure that this condition was achieved experimentally.

Numerical calculations of the temperature profile of the critical-current leads for measurements in liquid helium and the helium boil-off were performed using FlexPDE. The boundary conditions used in the time-dependent analyses were: $T(x = 0, t) = 4.2$ K and $T(x = L, t) = 300$ K. A J_c measurement is typically performed by ramping the current from zero up to above the transition, where the measured voltage is rapidly increasing. One measurement generally takes ~200 s before the current is set to zero and the probe is ready for the next measurement. The measurement time is predominantly determined by the n-value of the superconductor,[44] the time constant of the amplifier and the accuracy required for the measurement. Faster amplifiers can be used to reduce the measurement time. The ratio between the measuring time and the total time in one cycle is defined as a duty cycle (D). In this work, we consider the effects of duty cycle on the temperature profile and the average helium boil-off of the current leads and use a measuring time of 200 s for the applied current to reach the maximum value of I_{max}.

1. Without static or sample boil-off

Figure 7 illustrates the temperature profile of a brass current lead at 0 s, 200 s, and 1200 s (i.e., before the measurement, at the end of the measurement, and 1000 s after the mea-
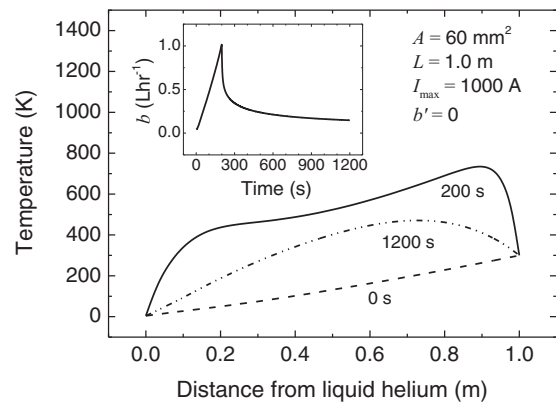

FIG. 7. Calculated temperature profile of a vapour-cooled brass current lead with the bottom end immersed in liquid helium while ramping the current up to a maximum current of 1000 A in 200 s and then reducing the current to zero without any static or sample boil-off ($b' = 0$). The current lead length is 1.0 m and the cross-sectional area is 60 mm². The inset shows the calculated helium boil-off as a function of time.

surement has finished) and the instantaneous helium boil-off (inset) during the first cycle where $A = 60$ mm², $L = 1.0$ m, $I_{max} = 1000$ A and there is no static or sample boil-off, i.e., $b' = (I^2R/c_l + m_{sta})/\delta_{liquid} = 0$ where δ_{liquid} is the density of liquid helium. We have used $b = m/\delta_{liquid}$ to represent helium boil-off measured in (useful experimental units of) L h⁻¹. To first order, b increases linearly with increasing current up to I_{max} and then slowly decays once the current is switched to zero due to the slow decrease in temperature back to equilibrium. The high temperature near the top end is up to 745 K. Hot current leads are not found for magnet current leads carrying a constant current in thermal equilibrium when helium boil-off is correctly minimized.[7]

Figure 8 shows the calculated average helium boil-off over 10 cycles for two current leads versus cross-sectional area as a function of applied current and duty cycle for $L = 1.0$ m. The average helium boil-off is approximately proportional to the maximum applied current. The data for $D = 0.5$ are re-plotted in Fig. 9 as b/I_{max} versus I_{max}/A, together with the calculated data for $L = 0.6$ m and 0.8 m. The optimized operation obtained at the minimum average helium boil-off is at $I_{max}/A = 5 \times 10^6$ A m⁻² for $L = 1.0$ m and at larger numbers for shorter current leads. The resulting maximum temperature (T_{max}) of the current lead is ~350 K as shown by the inset.

2. Tapered current leads

Since the heat leak into the liquid helium is a function of A (as given by Eq. (2)), we investigated the effects of making A smaller at the bottom end of the current leads and modelling heat flow in tapered current leads. The spatial dependence of A was taken to be $A(x) = A_{min} + \alpha x$ where α ranges from 20 to 140 mm²/m and A_{min} is the cross-sectional area at the bottom end. A range of calculated results is shown in Fig. 10 where b/I_{max} is plotted as a function of the maximum temperature. Calculated values for uniform A are also shown for comparison. Figure 10 shows that there is little difference between the uniform current leads and tapered current leads in
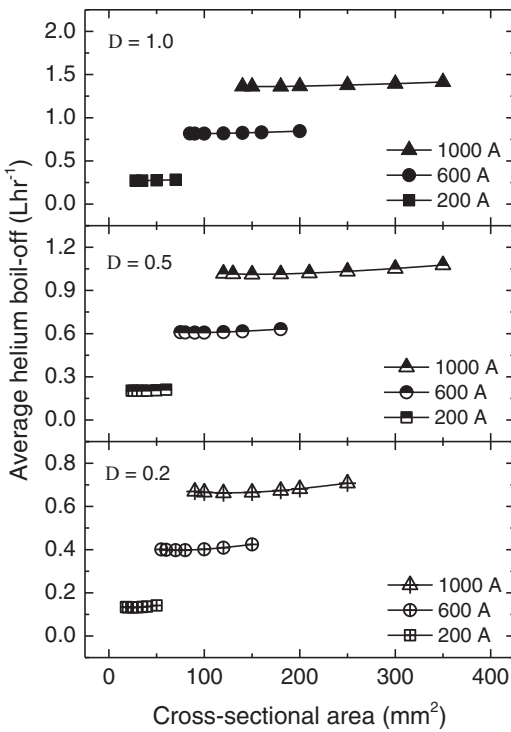
FIG. 8. Calculated average helium boil-off (averaged over 10 cycles) for two vapour-cooled brass current leads as a function of the cross-sectional area of each lead carrying a current up to 200, 600, and 1000 A for duty cycles of 0.2, 0.5, and 1.0. The system has no static or sample boil-off and the length of all current leads is 1.0 m.

terms of helium boil-off for any given maximum temperature. Reducing A increases the thermal resistance so that less heat is conducted into liquid helium when no current flows. However, once the current is applied, the consequent increase in the electrical resistance leads to larger heating especially at the bottom end. These two competing effects minimise the effects of cross-sectional area reduction. Hence, we conclude that making the current leads smaller at the bottom end to reduce the boil-off is not productive.
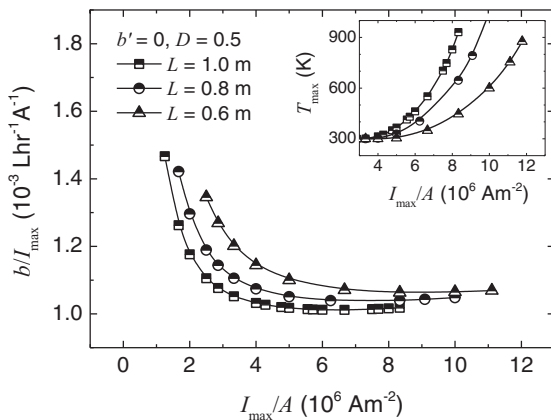

FIG. 9. Calculated average helium boil-off per unit current (b/I_{max}) for two vapour-cooled brass current leads and maximum temperature (inset) as a function of the ratio between the maximum current and cross-sectional area (I_{max}/A) of each lead without any static or sample boil-off for a duty cycle of 0.5 and current lead lengths of 0.6, 0.8, and 1.0 m.
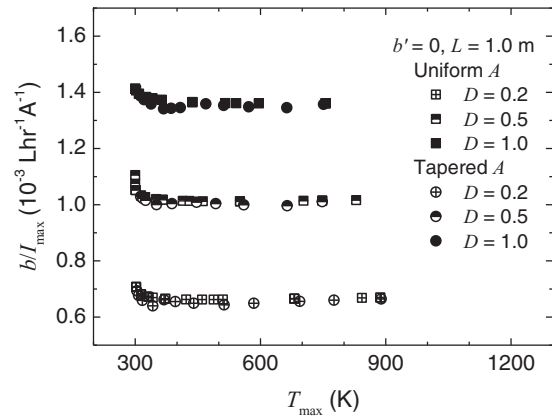

FIG. 10. Calculated average helium boil-off per unit current (b/I_{max}) for two vapour-cooled brass current leads as a function of maximum temperature with uniform cross-sectional area and tapered cross-sectional area. The system has no static or sample boil-off and the length of all current leads is 1.0 m.

3. Non-zero static boil-off

In most systems, there exists a static or sample boil-off which can be exploited in optimizing A. Figure 11 shows the average helium boil-off and maximum temperature (inset) as a function of I_{max}/A with a static boil-off (typically from the cryostat) and without static boil-off. We note one could optimize further by considering the boil-off from the cryostat and magnet at the lowest field (lowest boil-off) at which J_c is to be measured. The average static helium boil-off obtained from our horizontal magnet system is 0.3 $1h^{-1}$ which has been included in the calculations. Figure 11 shows that when the helium boil-off is minimized, T_{max} is larger than 400 K. These results and others (not shown) demonstrate that it is common that T_{max}, rather than the absolute minimum boil-off, often becomes the important limiting factor that determines the optimum A.
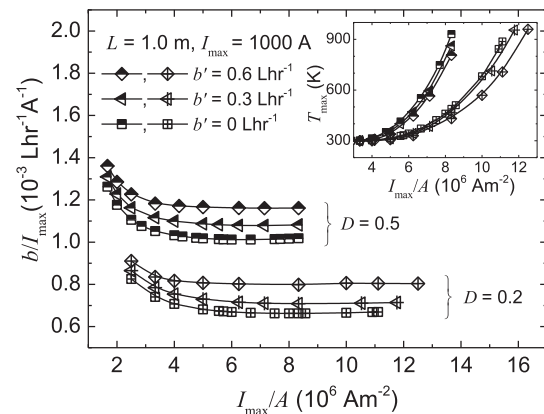

FIG. 11. Calculated average helium boil-off per unit current (b/I_{max}) for two vapour-cooled brass current leads and maximum temperature of the current leads (T_{max}—shown inset), as a function of the ratio between maximum current and cross-sectional area (I_{max}/A) of each lead with and without static or sample boil-off. The length of all current leads is 1.0 m. The maximum current investigated was 1000 A.
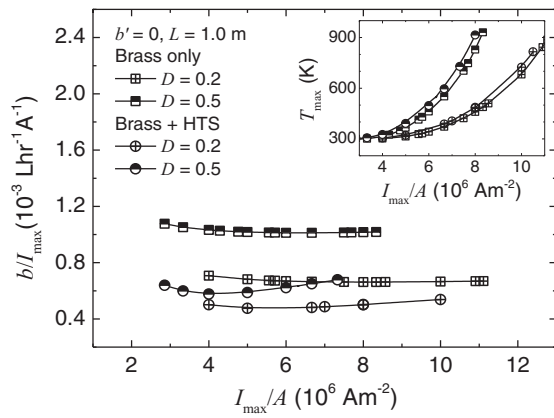
FIG. 12. Calculated average helium boil-off per unit current (b/I_{max}) for two vapour-cooled brass current leads and maximum temperature (inset) as a function of the ratio between maximum current and cross-sectional area (I_{max}/A) of each lead with and without HTS tapes at $x = 0$ m to $x = 0.5$ m from the total length of 1.0 m. The system has no static or sample boil-off.

4. Superconducting components of current leads

Adding some HTS along the current leads is useful in order to reduce Joule heating. Because in practice the amount of cryogen changes during experiments, it is not straightforward attaching the HTS tapes to the current leads while ensuring the temperature is always below the critical temperature of the component superconductor. Typically, one is conservative and the HTS is soldered to the current lead only near the bottom end. We have used YBCO coated conductor tape which has low thermal conductivity materials in its structure. The standard YBCO tape from SuperPower (SCS-type) has two 20-μm copper stabilizing layers and one 2-μm silver overlayer. The stabilizer-free tape (SF-type) has no copper which is useful for current lead applications. Five YBCO (SF4050) tapes were added into the calculations for $L = 1.0$ m from $x = 0$ m to $x = 0.5$ m, which is the position that the temperature is below the T_c of 93 K[45] in zero-current operation. The calculated average helium boil-off and maximum temperature for the hybrid current lead (brass and YBCO tapes) are shown in Fig. 12. The optimum A and resulting T_{max} are within ~10% of the brass current lead alone. Nevertheless, the helium boil-off is 30%–50% lower because the smaller Joule heating at the bottom end leads to a lower temperature gradient at $x = 0$ m.

5. Current lead cross-sectional-area (A)

When A is optimized for minimum helium boil-off, it is strongly dependent on the duty cycle of the measurement. Figure 13 shows that A decreases with decreasing duty cycle. For $D = 1$ and $b' = 0\,1\,h^{-1}$, the optimization of the brass critical-current leads gives

$$\frac{L I_{max}}{A} = 6.2 \times 10^6 \text{A m}^{-1}, \quad (4)$$

where $L = 1.0$ m. The helium boil-off from two current leads when D is unity is

$$\frac{b}{I_{max}} = 1.36 \times 10^{-3}\,1\,h^{-1}\,A^{-1}. \quad (5)$$

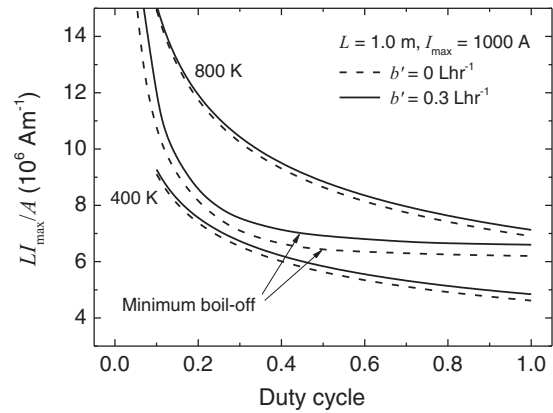
FIG. 13. Calculated optimum shape factors (LI_{max}/A) of a current lead for critical current measurements as a function of duty cycle for a static boil-off (b') of 0 and 0.3 l h^{-1} from Eq. (6) where the current-lead length is 1.0 m and the maximum current 1000 A. One data pair describe optimum conditions for the minimum average helium boil-off and the other two pairs show conditions when the maximum temperature of the current lead is the limiting factor, fixed at 400 K and 800 K.

Equation (5) gives about half the boil-off of that for brass magnet current leads which is $2.9 \times 10^{-3}\,1\,h^{-1}\,A^{-1}$ calculated from (1) and (2). However, the optimized critical-current lead runs hot—the temperature is above room temperature near the top end. Indeed, T_{max} of the critical-current leads becomes the critical optimization factor as shown in Fig. 13 where if the maximum safe temperature is 400 K, this condition is the important one at all values of duty cycle. Under the conditions that T_{max} is the limiting condition, one can use the empirical relation,

$$\frac{L I_{max}}{A} = \left[1.46 D^{-0.18} L^{0.4} (T_{max} - 300)^{0.25 D^{-0.09}} \right.$$
$$\left. + 750 \frac{b'}{I_{max}} D^{10^{-3} I_{max} - 2.87 b'} \right] \times 10^6 \text{A m}^{-1}, \quad (6)$$

which is accurate within ~18% where $0.1 \leq D \leq 1$, $T_{max} \geq 320$ K, $b' \leq 0.6\,1\,h^{-1}$ and $I_{max} \leq 1000$ A. For moderate duty cycle, Eq. (6) is most useful when T_{max} is less than ~450 K. At higher temperature, the calculated optimum LI_{max}/A from (6) is higher than the optimum LI_{max}/A obtained from the minimum boil-off, although the associated increase in helium boil-off rather small, less than 5%. A general empirical expression for boil-off accurate to ~14% is given by

$$\frac{b}{I_{max}} = (1.35 \times 10^{-3}) D^{0.41} (T_{max} - 300)^{-0.008}$$
$$+ 25 b'^{1.5} I_{max}^{-1.6}\,1\,h^{-1}\,A^{-1}. \quad (7)$$

Given $L = 1.0$ m for our magnet system and that $b' = 0.3\,1\,h^{-1}$, $D = 0.2$, and $T_{max} = 400$ K, the calculated optimum LI_{max}/A is 7.6×10^6 A m^{-1} for J_c measurements up to 1000 A. Comparing this optimum with the value from steady state calculation for magnet current leads of 2.0×10^6 A m^{-1} where the static boil-off and the duty cycle are not considered, the current leads optimized in this work reduce helium consumption from $1.0\,1\,h^{-1}$ to $0.7\,1\,h^{-1}$ (consistent with Fig. 11). Equation (7) has a weak T_{max} dependence and can be written in a form, when b' is small, that highlights that reduced duty

cycle reduces helium boil-off:

$$\frac{b}{I_{max}} \approx (1.35 \times 10^{-3})D^{0.41}\,\mathrm{l\,h^{-1}\,A^{-1}}. \qquad (8)$$

Furthermore, we have used HTS tapes at the lower part of the current leads to further reduce helium boil-off from Joule heating above and below the helium level. One can calculate the optimum cross-sectional area of the current lead using an L value at the minimum helium level (longest L) and put the HTS tapes above that level up to the maximum helium level (shortest L). Note in this work we have only considered vapour-cooled current leads used in measurements made with liquid helium. Design optimization of the current leads for other types of measurements, for example, in liquid nitrogen or using cryocooler technology, can be completed using a similar approach to that used here and starting with Eq. (1).

C. Temperature profile and gas flow measurements

Temperature profile measurements were performed along one of the vapour-cooled brass current leads to investigate to what degree the calculations agree with the experiments. The temperature profile was measured using five platinum resistance thermometers (standard PT 100) attached along the current lead every 20 cm from the top end (equivalent in Fig. 6 to putting thermometers at $x = L, L - 0.2, L - 0.4, L - 0.6,$ and $L - 0.8$ m from helium level). The thermometers were calibrated above 12 K in a Quantum Design Physical Properties Measurement System© and at 4.2 K in liquid helium. The effective length of the current leads was estimated from measuring the helium level in the cryostat using a cryogen level meter and the average helium gas flow along the current lead was monitored using a Techniquip MGF-420 gas flow meter calibrated for helium with the accuracy of 1.5%. The meter was an insertion-type so the pressure drop across it was negligible.

Figure 14 shows measurements of the temperature of a 10-mm^2 vapour-cooled brass current lead at $x = 0.18, 0.38, 0.58, 0.78,$ and 0.98 m from liquid helium as a function of
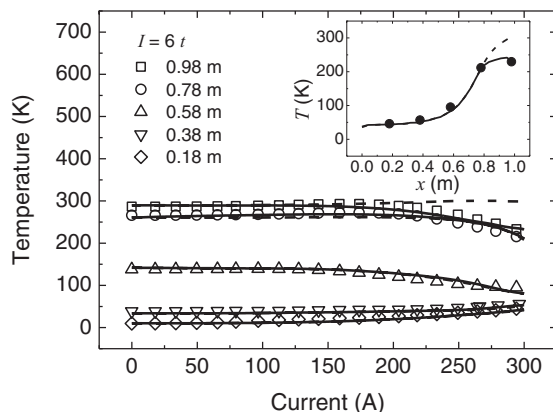

FIG. 14. Measurements of the temperature of a 10-mm^2 current lead as a function of applied current ramping at 6 A s^{-1} up to 300 A during the first cycle. The inset shows the temperature profile at 300 A. Dashed lines are calculations using Eqs. (1)–(3) with $m = \rho_{liquid}b$ from the experiment. Solid lines are calculations that include a convective-like cooling effect near the top end.

instantaneous current while it was ramped at 6 A s^{-1}. The relatively small A-value ensures we could easily measure heating effects. The broad features of the temperature profile are in agreement with the calculations in this work except in a small region close to the head of the probe. The inset shows the temperature profile of the current lead when the current was at 300 A. The dashed lines are calculated values which are in good agreement with the experimental data except for $x = 0.98$ m where the calculated temperature is higher than experiment. The data in Fig. 14 show the helium boil-off from Joule heating by elements immersed in the liquid helium correspond to a resistance (cf. R in Eq. (2)) of 4 mΩ. We attribute the increased cooling at the top end of the current leads than that found computationally to the complex nature of the helium gas convectively flowing within the head of the probe before leaving the system (shown in Fig. 1(a)) and the non-ideal thermal sinking of the leads at room temperature. The calculated Reynolds number is up to 3500 at 300 A which is a value in the transition region from laminar to turbulent flow.[46] We have assumed that the convectional cooling in the box is proportional to x and b with an additional proportionality constant as a free parameter and found that using $34.6bx$ from $x = L - 0.2$ m to $x = L$ m, which can be considered as characterizing convective heat transfer between the helium gas and the current lead where h and ΔT are proportional to b and x, respectively, improves agreement between calculation and experiment (cf. the solid lines of Fig. 14).

IV. VARIABLE-TEMPERATURE CUP

A. Design and calculations

Two designs of the variable-temperature cup with insulating plug and vent were produced and tested. The first design was made from Tufnol alone with the wall thickness of 6 mm. In the second design, the wall thickness of the Tufnol cup was reduced to 2 mm and a Spacetherm® aerogel blanket was used. In the latter case, the Tufnol helps provide mechanical support for the excellent insulation the aerogel provides. The thermal conductivity of the aerogel[47] is as low as 0.014 W m^{-1} K^{-1} at room temperature while the thermal conductivity of Tufnol is 0.37 W m^{-1} K^{-1}. The outer diameter of the cup was fixed at 32 mm. The design parameters are listed in Table II and a schematic of the second design (Tufnol + aerogel) of the variable-temperature cup is illustrated in Fig. 1(b). Figure 1(b) shows the current leads passed

TABLE II. Design parameters of the variable-temperature cups.

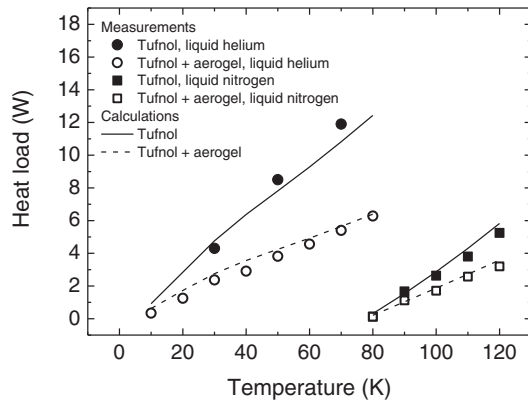| Parameter	1st design	2nd design
Tufnol thickness (mm)	6	2
Aerogel thickness (mm)	...	4
Internal cross-sectional area (mm^2)		
Cup + plug	314	314
Vent	78	38
Current lead		
Brass cross-sectional area (mm^2)	5	5
No. of YBCO tapes	5	3

FIG. 15. Measurements and calculations of the heat load in operation of the variable-temperature cup in the $J_c(B, T, \theta)$ probe as a function of the operating temperature in liquid helium and in liquid nitrogen.

through the cup at the top (which was sealed with epoxy) and through an insulating plug at the bottom that includes a vent for gas to escape when the temperature is increased (particularly important if the variable temperature enclosure has filled with cryogen and the heaters have just been turned on).[17] The temperature along the sample was measured with three Cernox thermometers (CX-1050-SD-1.4L) calibrated from 1.4 K to 325 K. The magnetic field-dependence of the thermometers was up to -0.16% at 20 K and 14 T and accounted for in setting the temperature. The temperature was controlled by two LakeShore 336 cryogenic temperature controllers with the resistive heater outputs. Three heaters were used to vary the sample's temperature. Two of them were made from a constantan wire noninductively wound on the OFHC copper block which was attached to the sample holder. The resistance of the two heaters was $51.2\ \Omega$ and $53.4\ \Omega$. Another heater with the resistance of $79.5\ \Omega$ was made by winding a constantan wire on a thin-wall cylindrical OFHC copper tube which was placed around the sample. Six layers of aluminized Mylar superinsulation were wrapped around the cylindrical heater tube in order to reduce the radiative heat transfer.

Heat transfer from the cup to the liquid cryogen reservoir is via conduction through the wall of the insulating cup as well as the insulating plug and the current leads, together with heat leak through the liquid/gas vent from liquid boil-off (cf. Fig. 1(b)). We have assumed there is no film boiling at the outer surfaces of the cup/plug/leads that are immersed in the cryogen. The heat transfer through the vent is complex. We have calculated it using a film boil-off heat transfer coefficient (h_b) that gives a convective-like heat transfer. We have taken

TABLE III. Calculated heat load of the variable-temperature cups in liquid helium.

Calculated heat load	1st design	2nd design
Average percentage (%)		
Cup + plug	51.8	24.7
Current leads	21.6	26.4
Vent	26.6	48.9
At 50 K (W)	7.8	4.2

the film boil-off heat transfer coefficient to be given by[48]

$$h_b = \left(\frac{4}{3}\right)^{3/4} \left(\frac{\kappa_V^3 \delta_V (\delta_L - \delta_V) g c_l}{H \eta_V \Delta T}\right)^{1/4}, \qquad (9)$$

where g is the standard gravity, H is the length of the heating surface (i.e., the length of the sample), η is the viscosity in $\mathrm{kg\,m^{-1}\,s^{-1}}$, and δ is the density in $\mathrm{kg\,m^{-3}}$. Subscripts L and V represent the liquid and vapour properties, respectively. The total heat load or power consumption of the
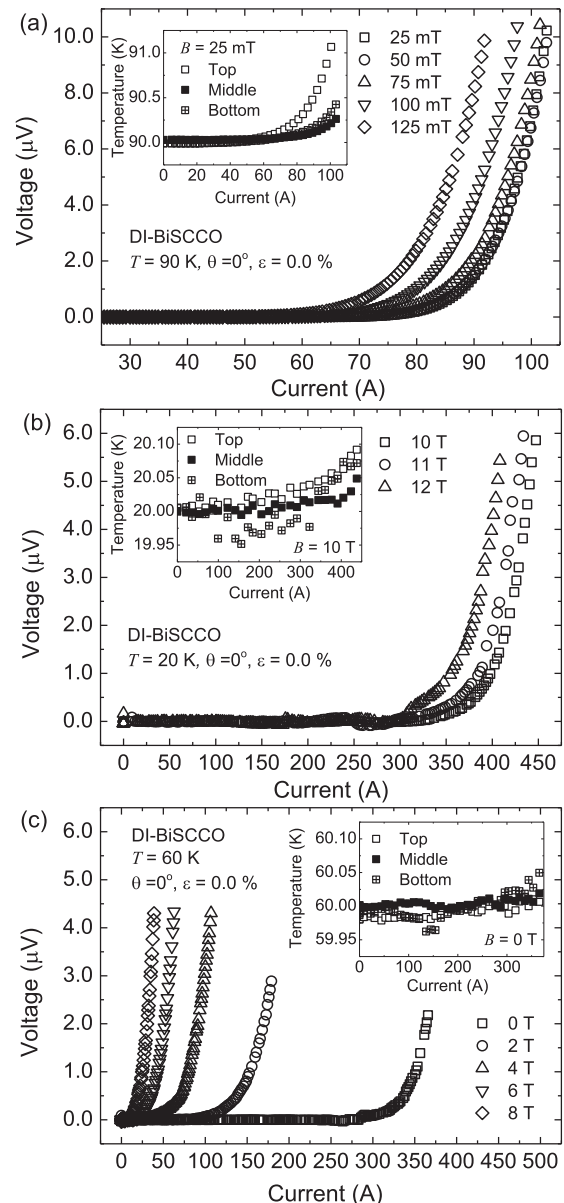

FIG. 16. (a) Voltage-current characteristics of a DI-BiSCCO tape at 90 K, measured as a function of applied magnetic field parallel to the tape surface for measurements in liquid nitrogen. The inset shows the temperature rising during the transition for the data taken at 25 mT where the critical current is 88 A at $100\ \mu\mathrm{V\,m^{-1}}$. ΔT across the voltage taps is 130 mK. (b) and (c) Voltage-current characteristics of the same sample at 20 K and 60 K as a function of applied magnetic field parallel to the tape surface for measurements in liquid helium. The insets show the temperature rising during the transition for data taken at 10 T at 20 K and 0 T at 60 K where the critical currents were 398 A and 352 A, respectively. In both cases, ΔT across the voltage taps is $\sim$30 mK.
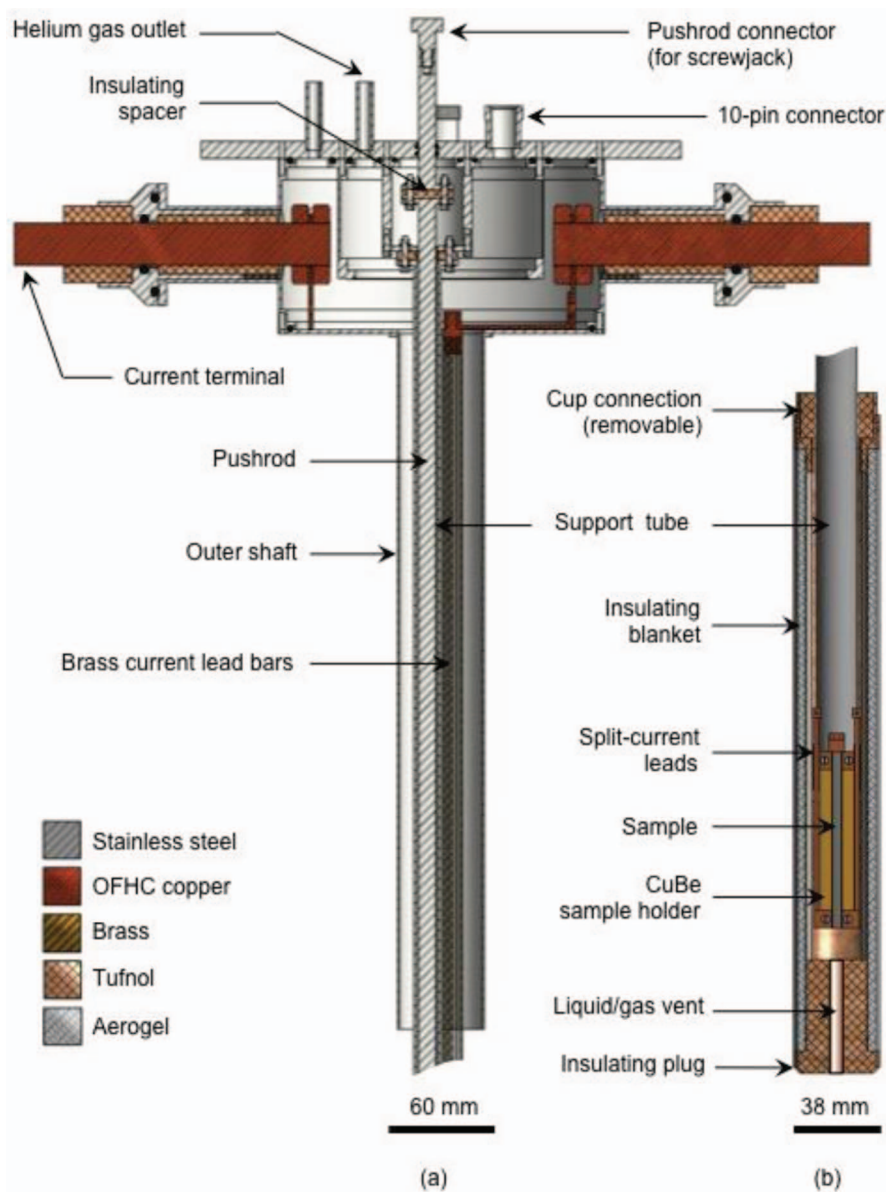
FIG. 17. Diagram of $J_c(B, T, \theta, \varepsilon)$ probe (a) the top part of the probe including a stack of brass current lead bars and (b) the variable-temperature cup, insulating plug and vent.

variable-temperature cup in liquid helium is given by

$$
P = \left(\kappa_t A_t \frac{\Delta T}{\Delta x} \right)_{cup} + \left(\kappa_t A_t \frac{\Delta T}{\Delta x} \right)_{current\ leads}
$$
$$
+ \left(\kappa_t A_t \frac{\Delta T}{\Delta x} \right)_{insulating\ plug} + h_b A_b (T - 4.2), \quad (10)
$$

where A_b is the effective area of the heating surface, and κ_t and A_t are the total overall thermal conductivity and cross-sectional area of the relevant multicomponent part. The calculated values are compared to the measured values in Fig. 15 as a function of operating temperature. We attribute the differences to uncertainties in the temperature dependence of thermal conductivity of component materials and the uncertain boil-off geometry. Table III shows the calculated heat load of the two designs of the cup at 50 K operating in liquid helium. The contribution from each type of heat transfer is shown as a

percentage of the total heat load. The major source of the heat transfer in the Tufnol design is conduction through the walls of the cup, which led to the use of the aerogel insulation in the second design. Other improvements include the reduction in the size of the vent and number of YBCO (SCS4050) tapes soldered on the bus bar current leads. All improvements together reduce the total heat load from 7.8 W to 4.2 W at 50 K. (equivalent to reducing helium consumption from 10.9 lh^{-1} to 5.9 lh^{-1}). The vent is the major source of boil-off in the 2nd design.

B. Variable-temperature measurements

The Tufnol + Spacetherm® aerogel variable-temperature cup was used to provide a variable-temperature environment for the J_c measurements on a DI-BiSCCO tape manufactured by Sumitomo Electric Industries. The J_c measurements were
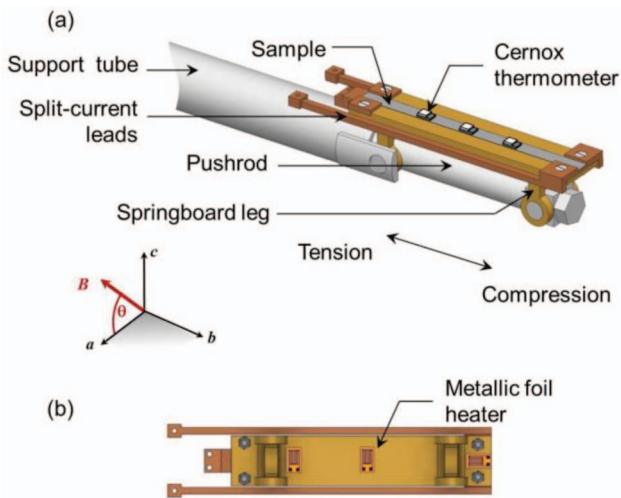
FIG. 18. (a) Diagram of the springboard-shaped sample holder and thermometry. (b) Metallic foil heaters underneath the sample holder.

carried out using a standard four-terminal technique with a pair of voltage taps 10-mm apart. The measurements were performed in liquid nitrogen in a conventional iron-cored electromagnet and in liquid helium in our 15 T vertical superconducting magnet. The temperature along the sample was monitored during the measurement to investigate the stability and variability of the temperature along the sample.

Figure 16 shows the voltage-current characteristics of the DI-BiSCCO tape as a function of magnetic field applied parallel to the tape surface for measurements in liquid nitrogen at 90 K and in liquid helium at 20 K and 60 K. The insets show the sample temperature measured at the top, the middle, and the bottom region of the sample during the J_c measurements. The initial temperatures are typically within 50 mK of the set point at the start of the measurements. Temperature control is such that at J_c there is an additional uncertainty of ∼30 mK across the voltage taps for measurements in liquid helium. The difference between the temperature and set point

is higher at the top and the bottom parts of the sample especially for measurements at 90 K in liquid nitrogen where ΔT is 130 mK. We attribute this to resistive heating in the YBCO current leads which enter the normal state at 93 K. Below 60 A, because one end of the YBCO current leads is at 77.4 K, resistive losses and hence the heating is relatively small. Once the current exceeds the temperature-dependent critical current of the YBCO tapes, Joule heating is enhanced. The inset in Fig. 16(a) shows this effect occurs sooner for the top current lead than the bottom because it is totally surrounded by Tufnol and the cooling relies only on the heat transfer by conduction. We note that the current leads can be re-optimized for J_c measurements above 90 K using DI-BiSCCO tapes if required.

V. DESCRIPTION OF $J_c(B, T, \theta, \varepsilon)$ PROBE

The $J_c(B, T, \theta, \varepsilon)$ probe was designed with the current leads optimized for our horizontal magnet system. The top and bottom parts of the probe are shown in Fig. 17 where the variable-temperature cup was modified to fit with the springboard-shaped sample holder. Figure 18 shows detailed apparatus of the springboard-shaped sample holder and thermometry. Split-current leads and heaters were made flexible due to a requirement of the strain measurements. All heaters were made from a metallic foil-type strain gauge on polyimide substrate and were initially installed underneath the sample holder for this work. The resistances of the as supplied gauges were 120 Ω.

Because of the stainless steel tubes that apply strain, the cylindrical shape was not practical for the vapour-cooled current leads. While brass was still used with all the benefits discussed above, the cylindrical shape was changed to a stack of brass bars. Each current lead for the $J_c(B, T, \theta, \varepsilon)$ probe was made from five of 1 mm × 10 mm × 1.0 m brass bars with 1.5-mm gaps between them. Four YBCO (SF4050) tapes were soldered to each current lead from the bottom (cryogenic) end up to $x = 0.5$ m. The total cross-sectional area of each current lead was ∼50 mm^2 which was the optimum for measurements
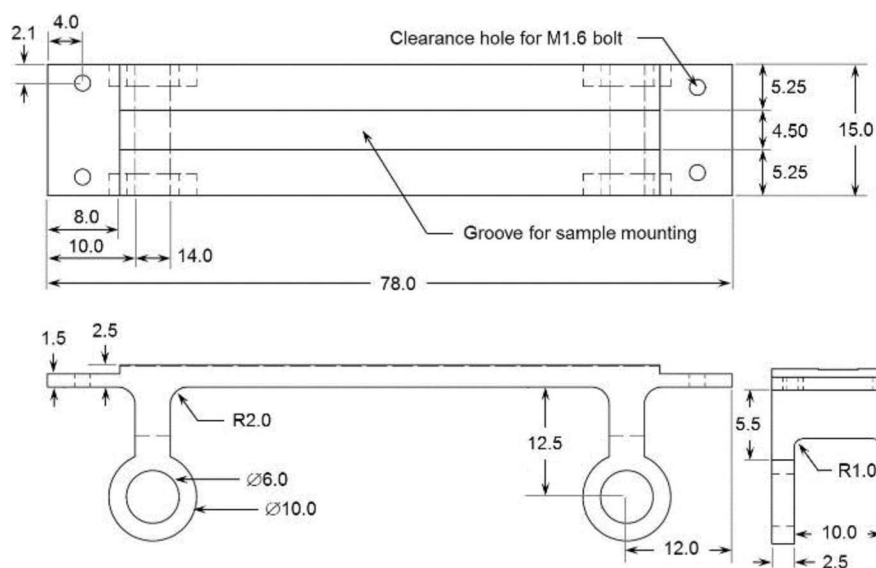

FIG. 19. Technical drawings of the springboard-shaped sample holder.

up to 425 A with $D = 0.2$, $T_{max} = 400$ K, and $b' = 0.3$ $1h^{-1}$. Since the probe was designed for variable-temperature measurements, additional boil-off from the cup will allow the probe to be operated to currents larger than 425 A. The observed static helium consumption of the probe alone was 0.5 $1h^{-1}$.

VI. STRAIN SAMPLE HOLDER

Strain was applied to the sample using the modified bending beam apparatus with the springboard-shaped sample holder. The sample holder was made from a copper beryllium alloy (Berylco 25) with good elastic properties, solderability, and relatively high resistivity.[1] It was 78 mm in length, 15 mm in width, and 2.5 mm in thickness, as shown in Fig. 19. The sample is soldered directly into a groove that runs along the length of the sample holder and ensures the superconducting component of the sample aligned with the top surface of the springboard and in the plane of the strain gauges. The final design ensures the springboard is long enough that we do not get current transfer voltages in our measurements. The wide surface of the springboard provides space for the strain gauge, Hall sensor and thermometry. The split-current leads were made from OFHC copper for measurements at liquid helium temperature. Four YBCO (SCS4050) tapes were used for each current lead for measurements in the variable-temperature cup. The pairs of legs at each end were pulled/pushed to adjust the strain on the top surface of the sample holder. The top pair was fixed to the support tube and the second pair to the solid pushrod. Uniaxial strains of -1.4% to 1.0% can be applied to the sample. Finite element analysis of the springboard-shaped sample holder with the applied strain of 1.08% is shown in Fig. 20. Strain homogeneities are better than 1 part in 10^5 across the thickness of the superconducting layer and also along the length of the sample between 10-mm voltage taps. In the strain measurements, strain gauges (Vishay WK series) are mounted on the sample holder next to the sample. This allows direct monitoring and active control of the strain during initial setup and measurements. At liquid helium temperature, the strain gauges exhibited a positive magnetoresistance of $\sim$180 mΩ at 14 T which corresponds to an effective

FIG. 21. Critical current density of a YBCO tape at 4.2 K as a function of applied strain for different magnetic fields normal to the tape surface.[4]

tensile strain of $\sim$0.025% relative to zero field. This magnetoresistance has been characterized and is accounted for during measurements. The total uncertainty in the measured strain is better than $\pm$0.02% for all the data taken.

VII. INVESTIGATION OF HTS TAPES

J_c measurements were performed on YBCO (SCS4050) tapes using the $J_c(B, T, \theta, \varepsilon)$ probe. The critical currents were defined using a 100 μV m^{-1} electric field criterion. Strain effects on the critical current density of the YBCO tape are presented in Fig. 21 for measurements in liquid helium and magnetic fields applied normal to the tape surface. At 4.2 K, the effects of strain on YBCO are weak and J_c is reversible over the strain range of -0.6% in compression to 0.3% in tension. We present J_c as a function of applied strain extended to -1.3% to illustrate the capability of our strain apparatus in measuring J_c in compression. We have not extended the measurements on YBCO up to the tensile limit of the springboard ($\sim$1.0%) to ensure we did not damage the sample. Figure 22 shows the magnetic field dependence of the critical current density for various angles between the fields and the tape surface at $\varepsilon = -0.03\%$. Data for $\varepsilon = -0.53\%$ and $\theta = 15°$ are also included. J_c of YBCO increases by a factor of 3 when θ
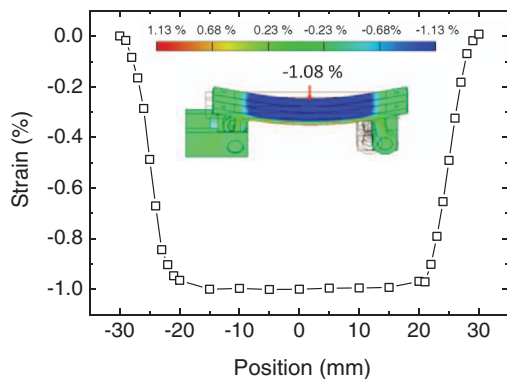

FIG. 20. Computational data of the strain homogeneity on the top surface of the 2.5-mm-thick springboard-shaped sample holder with an applied strain of -1.08%. The inset shows a colour plot of the data from finite element analysis.
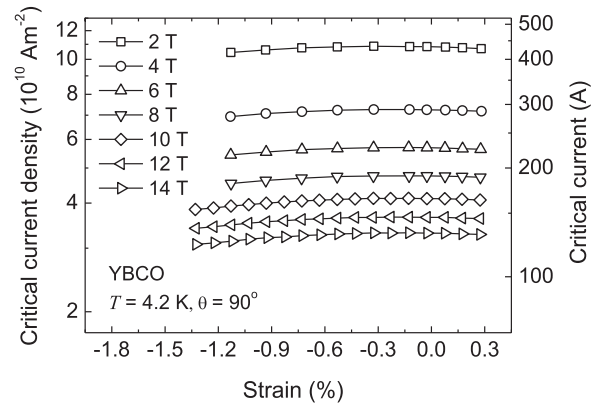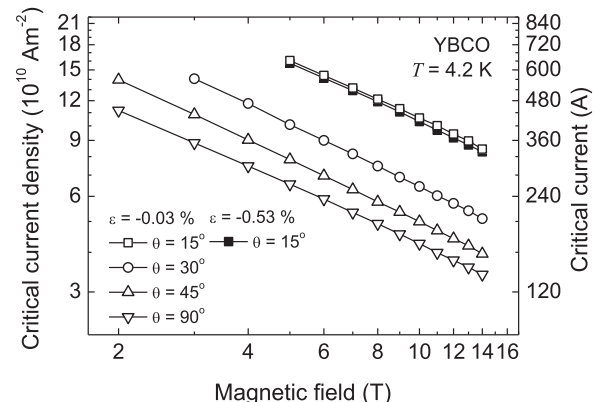

FIG. 22. Critical current density of a YBCO tape at 4.2 K as a function of applied magnetic field for different strains and angles between the magnetic field and the tape surface.[4]
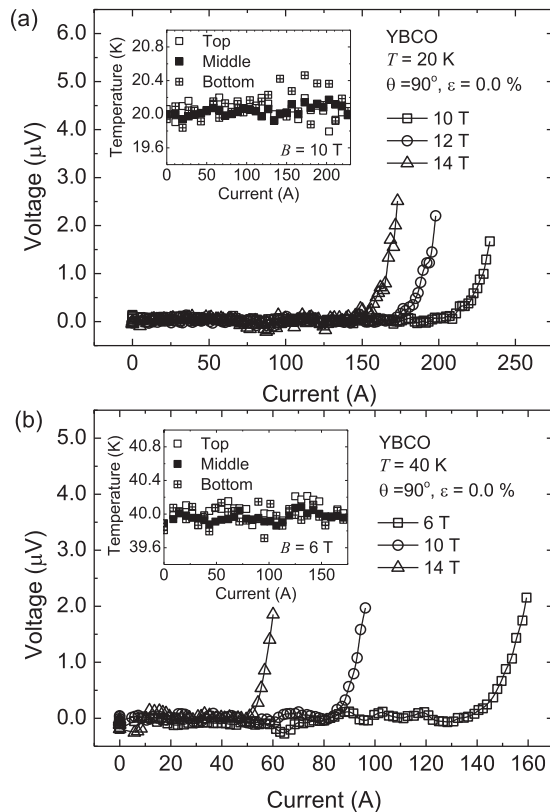
FIG. 23. (a) Voltage-current characteristics of a YBCO tape at 20 K, measured as a function of applied magnetic field normal to the tape surface for measurements in liquid helium. (b) Similar plots at 40 K. The insets show the temperature during the transition for data taken at 10 T at 20 K and 6 T at 40 K where the critical currents at 100 μV m^{-1} were 229 A and 153 A, respectively. In both cases, no systematic temperature increase was observed. The temperature variation was about ±150 mK.

changes from 90° to 15°. The anisotropy (Γ) of YBCO has been analysed based on anisotropic Ginzburg-Landau theory and $\Gamma = 7.0$ was found.[4]

In Fig. 23, voltage-current characteristics of the YBCO sample are shown at 20 K and 40 K for different magnetic fields applied normal to the tape surface when $\varepsilon = 0.0\%$. The inset data show that the temperature stability is sufficiently good that no significant change in temperature occurred during the transitions, either from heating of the sample or heating of the current leads made from YBCO tapes. However, the temperature variations are around ±150 mK which is higher than the $J_c(B, T, \theta)$ probe probably due to the larger volume of the variable temperature enclosure/sample space. Measurements using the variable-temperature cup were also performed as a function of strain at 40 K in the applied magnetic field of 6 T normal to the tape surface. Voltage-current characteristics are shown in Fig. 24 (inset) for the applied strains of 0.0%, −0.3%, and −0.6%. The noise in the base line of the measurements was several hundred nanovolts peak-to-peak which we attribute to the stability of the temperature control. The critical current density obtained as a function of strain at 6 T and 4.2 K has been normalized and plotted in Fig. 24, together with two other temperatures for comparison. An explanation of increased strain sensitivity with increased temperature observed here requires an understanding of how
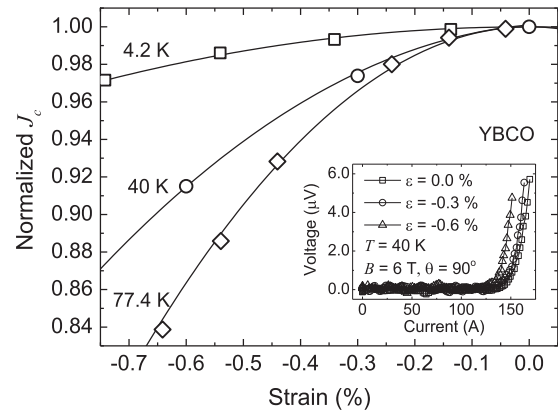

FIG. 24. Normalized critical current density of YBCO tapes as a function of strain at 4.2 K, 40 K, and 77.4 K and 6 T. The inset shows voltage-current characteristics of a YBCO tape at 40 K as a function of applied strain with the magnetic field applied normal to the tape surface.

strain affects the normal state resistivity of grain boundaries in the YBCO sample.[4] We are confident that the variations in temperature can be reduced if necessary with further optimization of the feedback circuit (i.e., proportional-integral-differential (PID) parameters). These J_c results confirm the probe operates successfully.

VIII. CONCLUSIONS

We have successfully designed, constructed, and commissioned a probe for $J_c(B, T, \theta, \varepsilon)$ measurements on high temperature superconductors. The probe was designed and optimized for Durham's split-pair horizontal magnet system. Design considerations and detailed calculations have been discussed and a generalized solution for optimization of the vapour-cooled brass current leads produced. The optimum cross-sectional area of the critical-current leads has been calculated and includes consideration of the duty cycle of the measurements, the static helium consumption of the cryostat, and the maximum safe temperature of the leads since by allowing the leads to run hot, we consume less cryogen. This work shows that beyond the special case of magnet current leads continuously running at constant current, more generally one can expect that hot current leads will be most efficient for cryogenic applications. The probe used an insulating enclosure for the variable-temperature measurements. The total uncertainty of the sample's temperature during J_c measurements was typically ~0.1 K. This was influenced by the design and thermometry of the probe and the control system. Uniaxial compressive and tensile strains were obtained using the springboard-shaped sample holder. Strains of −1.4% to 1.0% can be applied with a total uncertainty of the measured strain better than $\pm0.02\%$.

ACKNOWLEDGMENTS

[1] N. Cheggour and D. P. Hampshire, "A probe for investigating the effects of temperature, strain, and magnetic field on transport critical currents in superconducting wires and tapes," Rev. Sci. Instrum. **71**, 4521–4530 (2000).

[2] A. Godeke *et al.*, "A device to investigate the axial strain dependence of the critical current density in superconductors," Rev. Sci. Instrum. **75**, 5112–5118 (2004).

[3] D. M. J. Taylor and D. P. Hampshire, "Properties of helical springs used to measure the axial strain dependence of the critical current density in superconducting wires," Supercond. Sci. Technol. **18**, 356–368 (2005).

[4] P. Sunwong, J. S. Higgins, Y. Tsui, M. J. Raine, and D. P. Hampshire, "The critical current density of grain boundary channels in polycrystalline HTS and LTS superconductors in magnetic fields," Supercond. Sci. Technol. **26**, 095006 (2013).

[5] J. H. Durrell *et al.*, "Dependence of critical current on field angle in off-c axis grown Bi2Sr2CaCu2O8," Appl. Phys. Lett. **77**, 1686 (2000).

[6] W. J. Nuttall, R. H. Clarke, and B. A. Glowacki, "Stop squandering helium," Nature **485**, 573 (2012).

[7] M. N. Wilson, *Superconducting Magnets* (Oxford University Press, 1986).

[8] H. Lee, P. Arakawa, K. R. Efferson, and Y. Isawa, "Helium vapour-cooled brass current leads: Experimental and analytical results," Cryogenics **41**, 485–489 (2001).

[9] S. Jeong and S. In, "Investigation on vapor-cooled current leads operating in a pulse mode," Cryogenics **44**, 241–248 (2004).

[10] L. F. Goodrich, D. F. Vecchia, E. S. Pittman, J. W. Ekin, and A. F. Clark, *Standard Reference Materials: Critical Current Measurements on an NbTi Superconducting Wire Standard Reference Material* (NBS Special Publication, Boulder, 1984), pp. 1–54.

[11] H. A. Hamid and D. P. Hampshire, "Critical current density of superconductors as a function of strain in high magnetic fields," Cryogenics **38**, 1007–1015 (1998).

[12] T. Hasebe *et al.*, "Critical current measurement unit utilizing Bi-based oxide superconducting current leads and cryocoolers," IEEE Trans. Appl. Supercond. **5**, 821–824 (1995).

[13] M. A. Young *et al.*, "Measurements of the performance of BSCCO HTS tape under magnetic fields with a cryocooled test rig," IEEE Trans. Appl. Supercond. **13**, 2964–2967 (2003).

[14] M. H. Sohn *et al.*, "Development of cryogen free I_c measurement system," Physica C **468**, 2161–2164 (2008).

[15] L. F. Goodrich, L. T. Medina, and T. C. Stauffer, "High critical-current measurements in liquid and gaseous helium," Adv. Cryog. Eng. **44**, 873–880 (1998).

[16] J. W. Ekin, *Experimental Techniques for Low-Temperature Measurements* (Oxford University Press, New York, 2007).

[17] D. C. van der Laan, H. J. N. van Eck, J. Schwartz, B. ten Haken, and H. H. J. ten Kate, "Interpretation of the critical current in $Bi_2Sr_2Ca_2Cu_3O_x$ tape conductors as parallel weak-link and strong-link paths," Physica C **372–376**, 1024–1027 (2002).

[18] J. Ekin, "Strain scaling law for flux pinning in practical superconductors. Pt. 1: Basic relationship and application to Nb_3Sn conductors," Cryogenics **20**, 611–624 (1980).

[19] K. Osamura *et al.*, "Mechanical behavior and strain dependence of the critical current of DI-BSCCO tapes," Supercond. Sci. Technol. **21**, 054010 (2008).

[20] K. Osamura, "Force free strain exerted on a YBCO layer at 77 K in surround Cu stabilized YBCO coated conductors," Supercond. Sci. Technol. **23**, 045020 (2010).

[21] C. R. Walters, I. M. Davidson, and G. E. Tuck, "Long sample high sensitivity critical current measurements under strain," Cryogenics **26**, 406–412 (1986).

[22] N. Cheggour and D. P. Hampshire, "Unifying the strain and temperature scaling laws for the pinning force density in superconducting niobium-tin multifilamentary wires," J. Appl. Phys. **86**, 552–555 (1999).

[23] S. A. Keys, N. Koizumi, and D. P. Hampshire, "The strain and temperature scaling law for the critical current density of a jelly-roll Nb_3Al strand in high magnetic fields," Supercond. Sci. Technol. **15**, 991–1010 (2002).

[24] D. Taylor and D. Hampshire, "The scaling law for the strain dependence of the critical current density in Nb_3Sn superconducting wires," Supercond. Sci. Technol. **18**, S241–S252 (2005).

[25] W. Fietz and W. Webb, "Hysteresis in superconducting alloys—Temperature and field dependence of dislocation pinning in niobium alloys," Phys. Rev. **178**, 657–667 (1969).

[26] R. G. Hampshire and M. T. Taylor, "Critical supercurrents and the pinning of vortices in commercial Nb-60 at% Ti," J. Phys. F: Met. Phys. **2**, 89–106 (1972).

[27] X. F. Lu, D. M. J. Taylor, and D. P. Hampshire, "Critical current scaling laws for advanced superconducting strands for fusion applications with six free parameters," Supercond. Sci. Technol. **21**, 105016 (2008).

[28] D. P. Hampshire, H. Jones, and E. W. J. Mitchell, "An in-depth characterisation of $(NbTa)_3Sn$ filamentary superconductor," IEEE Trans. Magn. **21**, 289–292 (1985).

[29] L. Bottura and B. Bordini, "$J_C(B, T, \varepsilon)$ parameterization for the ITER Nb_3Sn production," IEEE Trans. Appl. Supercond. **19**, 1521–1524 (2009).

[30] S. A. Keys and D. P. Hampshire, "A scaling law for the critical current density of weakly and strongly-coupled superconductors, used to parameterise data from a technological Nb_3Sn strand," Supercond. Sci. Technol. **16**, 1097–1108 (2003).

[31] G. Carty and D. P. Hampshire, "Visualising the mechanism that determines the critical current density in polycrystalline superconductors using time-dependent Ginzburg-Landau theory," Phys. Rev. B **77**, 172501 (2008).

[32] D. Dew-Hughes, "Flux pinning mechanisms in type II superconductors," Philos. Mag. **30**, 293–305 (1974).

[33] E. J. Kramer, "Scaling laws for flux pinning in hard superconductors," J. Appl. Phys. **44**, 1360–1370 (1973).

[34] B. ten Haken and H. H. J. ten Kate, "Compressive and tensile axial strain reduced critical currents in Bi-2212 conductors," IEEE Trans. Appl. Supercond. **5**, 1298–1301 (1995).

[35] B. ten Haken, A. Godeke, H. H. J. ten Kate, and W. Specking, "The critical current of Nb_3Sn wires for ITER as a function of the axial tension and compression," IEEE Trans. Magn. **32**, 2739–2742 (1996).

[36] B. ten Haken, A. Godeke, and H. H. J. ten Kate, "The strain dependence of the critical properties of Nb_3Sn conductors," J. Appl. Phys. **85**, 3247–3253 (1999).

[37] J. W. Ekin, "Current transfer in multifilamentary superconductors. I. Theory," J. Appl. Phys. **49**, 3406–3409 (1978).

[38] J. W. Ekin, "Current transfer in multifilamentary superconductors. II. Experimental results," J. Appl. Phys. **49**, 3410 (1978).

[39] J. H. Duyn, "The future of ultra-high field MRI and fMRI for study of the human brain," Neuroimage **62**, 1241 (2012).

[40] C. Sborchia *et al.*, "Overview of ITER magnet system and European contribution," in IEEE/NPSS 24th Symposium on Fusion Engineering, S03D-l (2011).

[41] S. A. Keys and D. P. Hampshire, "Characterisation of the transport critical current density for conductor applications, in *Handbook of Superconducting Materials*, edited by D. Cardwell and D. Ginley (IOP Publishing, Bristol, 2003), Vol. 2, pp. 1297–1322.

[42] P. Sunwong, J. S. Higgins, and D. P. Hampshire, "Critical current measurements of DI-BSCCO tapes as a function of angle in high magnetic fields," J. Phys.: Conf. Ser. **234**, 022013 (2010).

[43] G. Morgan, "Optimization of current leads into a cryogenic system," Brookhaven National Laboratory Report AADD-171, 1970.

[44] D. M. J. Taylor, S. A. Keys, and D. P. Hampshire, "*E-J* characteristics and *n*-values of a niobium-tin superconducting wire as a function of magnetic field, temperature and strain," Physica C **372**, 1291–1294 (2002).

[45] M. K. Wu *et al.*, "Superconductivity at 93 K in a new mixed-phase Y-Ba-Cu-O compound system at ambient pressure," Phys. Rev. Lett. **58**, 908–910 (1987).

[46] J. P. Holman, *Heat Transfer* (McGraw-Hill, 2002).

[47] A. Lyons, *Materials for Architects and Builders* (Elsevier Ltd., 2010).

[48] C. E. Brennen, *Fundamentals of Multiphase Flow* (Cambridge University Press, 2005).

[49] See http://cryogenics.nist.gov/MPropsMAY/materialproperties.htm for thermal conductivity and specific heat capacity (2013).

[50] See www.tufnol.com for properties of tufnol (2008).

[51] See www.proctorgroup.com/products/thermal-insulation/spacetherm for properties of aerogel (2010).

[52] See http://webbook.nist.gov/chemistry/fluid/ for helium and nitrogen gases (2011).